PAPER

Check for updates

Zeolitization of fly ash for synthesis of pharmaceutically important bis(indolyl)methane derivatives

Aashima Mahajan,[a] Loveleen K. Brar ID *[b] and Manmohan Chhibber ID *[a]

Waste valorization represents an essential strategy toward achieving sustainable development goal 12 (Responsible Consumption and Production). In this work, coal fly ash was successfully transformed into Zeolite A and employed as a heterogeneous catalyst for the synthesis of pharmaceutically relevant bis(indolyl)methane derivatives (BIMs). Structural and morphological studies, conducted using X-ray diffraction (XRD) and field-emission scanning electron microscopy (FESEM), confirmed the formation of Zeolite A (ZA). Acid modification with 0.01 M HCl for 30 minutes at 60 °C resulted in ZA2/30, the most active catalyst among the five synthesized. The ZA2/30 exhibited enhanced surface area (56.1 to 66.2 m^2 g^{-1}) and pore size (5.4 to 6.3 nm) compared to ZA. Ammonia temperature programmed desorption (NH_3-TPD), Fourier transform infrared (FTIR) and X-ray photoelectron spectroscopy (XPS) analyses revealed an increase in the concentration of Brønsted acid sites with decreasing Si/Al ratio, which directly correlated with improved catalytic activity. The optimized catalyst enabled the synthesis of BIMs in yields ranging from 44% to 94%, under mild and environmentally friendly conditions. The used catalyst was studied for reusability up to five cycles. Leaching studies confirmed the heterogeneous nature of the catalyst, demonstrated its structural stability and reusability during successive cycles. This study establishes fly ash-derived zeolites as eco-friendly catalysts for sustainable organic synthesis, reinforcing their role in advancing circular chemistry.

1. Introduction

The continuously rising demand for energy has resulted in the extensive utilization of coal in thermal power plants, leading to large-scale production of coal fly ash. Each year, approximately 600–800 million tons of fly ash is produced worldwide,[1] of which only approximately 30% is utilized in sectors such as cement, concrete, road construction, and brick manufacturing. The remaining fly ash is disposed of in open pits, which leads to leaching of heavy metals into the soil, causing environmental pollution and posing serious health risks.[2]

The rich chemical composition of fly ash, including silicon oxide, aluminium oxide, trace alkali metal oxides and iron oxide, has remained largely underutilized.[3] Recent studies have exploited these components for synthesizing aerogels,[4] metal–organic frameworks (MOFs),[5] zeolites[6] and nanocomposites.[7] These value-added products synthesized from fly ash have

been utilized in biodiesel production,[8] organic reactions,[9] degradation of drugs,[10] dyes,[7] polymers[11] and volatile organic compound remediation.[12]

Zeolites derived from abundant feedstocks, such as coal fly ash, rice husk,[13] and coal bottom ash,[14] address sustainability concerns while serving as solid-state catalysts in organic synthesis. They have high thermal stability, defined pore structures, high surface areas, and low production costs, making them attractive alternatives for heterogeneous catalysis.[15,16] These zeolites find use as catalysts in reactions such as Michael addition,[9] Friedel–Crafts acylation,[17] Claisen–Schmidt condensation,[18] and Knoevenagel condensation reactions.[19]

Bis(indolyl)methanes (BIMs), a class of bioactive molecules, are secondary metabolites found in various natural sources, like cruciferous vegetables, marine life, and terrestrial organisms.[20] Fig. 1 shows the structure of some BIMs known for their anti-tumor, antibiotic, and antiviral activities.[21] Traditionally, these molecules were synthesized using conventional organic methods, but a number of homogeneous and heterogeneous catalysts, such as MOFs,[22] enzymes,[23] nanomaterials,[24] ultrasound,[25] metal oxides or complexes supported on alumina or graphene oxide,[26,27] and ionic liquids[28] have been reported recently.

[a] *Department of Chemistry and Biochemistry, Thapar Institute of Engineering and Technology, Patiala, 147004, Punjab, India. E-mail: mchhibber@thapar.edu*
[b] *Department of Physics and Material Science, Thapar Institute of Engineering and Technology, Patiala, 147004, Punjab, India. E-mail: brarloveleen@thapar.edu*
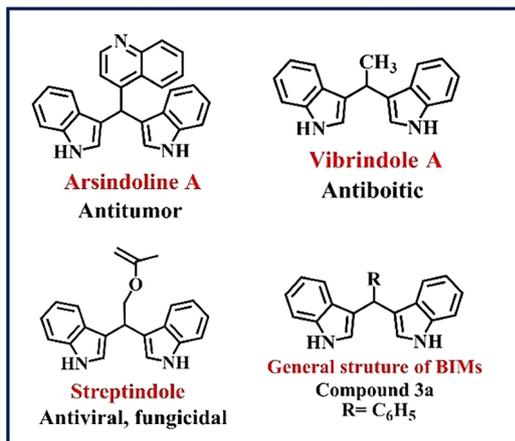
Fig. 1 Molecular structure of some biologically active bis(indolyl)-methanes (BIMs) and their general structure.

Although the above catalysts are efficient, environmental concerns and high costs necessitate the development of sustainable and eco-friendly alternatives.

This work uniquely employs fly ash—an abundantly available industrial by-product—as a feedstock to synthesize Zeolite A, thereby converting waste into a value-added material. Furthermore, treating Zeolite A with mineral acid added worth to the material, making it a heterogeneous catalyst for BIM synthesis with a Turnover number (TON) of 95.5 and Turnover frequency (TOF) of 3.9. In contrast, previous studies reported the use of mineral and organic acids along with transition metals to modify the commercial zeolites (HY, Hβ, and H-ZSM-5) for the synthesis of BIMs.[29–33] Notably, TOF and TON metrics for the zeolite-catalyzed synthesis of BIMs have not been reported in previous literature. Thus, to the best of our knowledge, this study reports the first use of a mineral acid-treated, fly ash-derived zeolite as a catalyst for ethanol-mediated BIM synthesis. Ethanol, compared to chlorinated solvents, as used in earlier reports,[29–33] is safe, biodegradable, and renewable. Overall, this work demonstrates a reduction in dependence on virgin raw materials, such as high-purity silica and alumina, by effectively utilizing fly ash waste, thereby diverting it from landfills and complying with SDG 12 – responsible consumption and production.

2. Materials and methods

2.1 Materials

Coal fly ash (CFA) used as the precursor material in this work was collected from Guru Gobind Singh Super Thermal Power Plant, Ropar (Punjab), India. Sodium hydroxide (Loba Chemie, 97%) and sodium aluminate (Otto Chemika Biochemika) were employed directly without further purification. Distilled water was used for all washing and dilution procedures. The suspended material from the dispersions was collected using a centrifuge (Thermo Fisher Scientific, 8000 rpm), and the aging process was carried out using an ultrasonic probe (ChromTech,

100 W/220 V/5 A). Fly ash was reduced to fine particles using a planetary ball mill (Mechmin).

For the synthesis of bis(indolyl)methane (BIMs), benzaldehyde, indole and solvent were procured from Avra, Loba Chemie, and Sigma Aldrich. The progress of the reaction was monitored using thin-layer chromatography (TLC; Silica gel 60 F254, Merck), and the purification was done using column chromatography.

2.2 Instruments and characterization

The characterization of the prepared samples was carried out using the following instruments. Morphological analysis was performed using a field-emission scanning electron microscope (FE-SEM; Carl Zeiss Sigma 500 FEG-SEM) operated at 20 kV, while elemental composition was analyzed using an energy-dispersive X-ray spectrometer (EDX; Bruker QUANTAX 200). The structural characteristics of the synthesized zeolite were examined using X-ray diffraction (XRD; Smart Lab SE, Rigaku) with Cu Kα radiation ($\lambda = 1.54$ Å). Diffraction patterns were recorded across a 2θ range of $5°$ to $80°$, with a step size of $0.013°$. Fourier transform infrared spectroscopy (FTIR; Bruker Alpha II) was used to identify functional groups in the samples over the spectral range of 400–4000 cm^{-1}. Thermal stability and decomposition behavior were analyzed by thermogravimetric analysis (TGA; NETZSCH STA 449 F3 Jupiter) up to 800 °C at a heating rate of 10 °C min^{-1} under a nitrogen atmosphere. The surface composition and elemental states were determined using X-ray photoelectron spectroscopy (XPS; PHI 5000 Versa Probe II, FEI Inc.) with Al Kα radiation (1486.7 eV) and silver as the reference standard. After degassing the samples at 100 °C, specific surface areas and pore distribution were evaluated from nitrogen adsorption–desorption isotherms using the Brunauer–Emmett–Teller (BET) and Barrett–Joyner–Halenda (BJH) models (Micromeritics ASAP 2020). The point of zero charge (PZC) for the synthesized zeolites was calculated using a previously reported method.[34] The acidity of the samples was determined by NH$_3$ temperature-programmed desorption (NH$_3$-TPD) using a chemisorption analyzer (BELCAT II, MicrotracBEL). Prior to analysis, samples were pretreated under helium, followed by NH$_3$ adsorption. The desorption process was then carried out by heating the samples from 100 to 800 °C at a rate of 10 °C min^{-1}, while the released gases were detected using a thermal conductivity detector (TCD). The heterogeneous nature and stability of the catalyst were examined through microwave plasma–atomic emission spectroscopy (MP-AES; Agilent 4100).

The synthesized organic compounds, BIMs, were characterized using a ^{1}H and ^{13}C nuclear magnetic resonance spectrometer (NMR, 400 MHz, JEOL) and CDCl$_3$ as the solvent. The molecular weights of the synthesized organic compounds were confirmed using high-resolution mass spectrometry (HRMS; Waters XEVO-G2XSQTOF).

2.3 Pretreatment of fly ash

CFA (4 g) was washed with water (3 × 200 mL) to remove water-soluble impurities and dried in an oven at 90 °C. To remove

volatiles, the dried CFA was calcinated at 800 °C (5 °C min^{-1}) for 2 h. Furthermore, metallic impurities were removed from the calcinated material by treating it with a 10% HCl solution (100 mL), followed by washing with water until neutral pH. It was then dried overnight in an oven at 90 °C, and the obtained material was designated as P-FA.

2.4 Reduction of particle size

To reduce the particle size, 20 g of the prepared P-FA was milled in a planetary ball mill using tungsten carbide jars and tungsten carbide balls. The material (P-FA) was milled with a ball-to-powder weight ratio of 20:1 for 30 h at 300 rpm, with toluene as the medium to minimize heat generation. Sodium lauryl sulfate (200 mg) was used as a surfactant to prevent agglomeration during the milling process. After milling was complete, toluene was decanted, and the residual solvent was evaporated by heating at 120 °C. It was then washed with a 1:1 ratio of water:ethanol (6 × 25 mL) to remove the surfactant and trace amounts of toluene. After drying at 120 °C, the product was sieved through a 200-mesh sieve to obtain an even particle size distribution and was referred to as B-FA.

2.5 Synthesis of Zeolite A

Zeolite A was synthesised from B-FA *via* an ultrasonication-assisted hydrothermal approach using a known procedure with slight modification.[35] B-FA (Si/Al is 1.4:1 determined using XRD[36]) was combined with NaOH (1:1.4) and sodium aluminate (to adjust the Si:Al ratio to 1:1) using a pestle and mortar. The mixture was then fused in a nickel crucible at 750 °C for 2 h in a muffle furnace. After cooling to room temperature, the fused product was ground into a fine powder and dispersed in water (2 g/20 mL). The resulting suspension was aged at room temperature for 3 h using an ultrasonic probe. Subsequently, the suspension was transferred into a Teflon-lined stainless steel autoclave and heated at 90 °C for 10 h. The crystalline product was collected, thoroughly washed with water until a

pH of 7 was achieved, and dried at 80 °C (Fig. 2). The resulting product was designated as ZA.

2.6 Acid-treated Zeolite A: pathway to ZA2/30

ZA (120 mg) was treated with 20 mL of 0.01 M HCl and stirred in a round-bottom flask for 30 min to enhance its surface area. The acid-treated ZA was then collected, washed repeatedly with water (five times) until a neutral pH was reached, and dried at 80 °C for 10 hours. The sample obtained was referred to as ZA2/30 and characterized using XRD, FE-SEM, EDS, TGA, FTIR, BET, XPS, and NH$_3$-TPD. NH$_3$-TPD analysis provided information on the total acid sites of the zeolite, which was used to calculate the turnover number (TON) and turnover frequency (TOF), thereby directly correlating acidity with catalytic performance.

2.7 Reusability studies

The reusability studies were carried out after recovering the used catalyst from the organic reaction mixture. The procedure for setting up the organic reaction mixture is described in Section 2.8.

2.7.1 Catalyst recovery and treatment.
After each reaction cycle, the zeolite ZA2/30 catalyst was separated from the reaction mixture using centrifugation. Each time the catalyst was washed with a 60:40 water–ethanol mixture (6 × 15 mL) and stirred in 20 mL of the same solvent ratio at 60 °C for 2 h to remove any residual organic compounds. The recovered solid was dried overnight at 80 °C in a hot-air oven, and characterization (XRD and FE-SEM, Fig. S6) was performed before reuse in subsequent organic reactions.

2.7.2 Leaching studies.
The supernatant obtained after catalyst separation was collected to assess possible leaching of framework elements. The ethanol was evaporated to dryness, yielding a residue of ~250 mg. This residue was transferred to a 50 mL volumetric flask, dissolved in a mixture of 5 mL concentrated HCl and 45 mL deionized water, and analyzed by MP-AES to determine the Si and Al content.
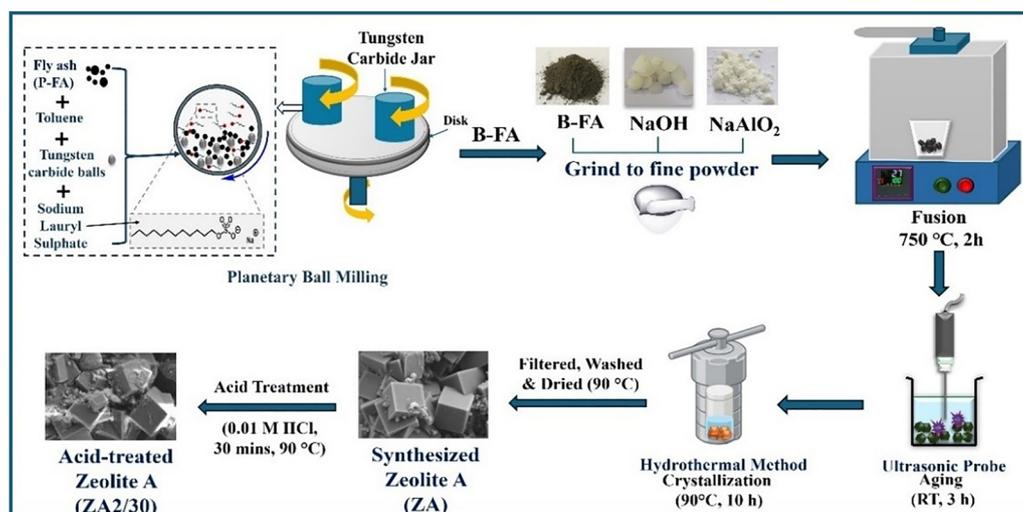

Fig. 2 Schematic representation of zeolite synthesis from ball-milled fly ash using an ultrasonic-assisted hydrothermal method.

2.8 General procedure for the synthesis of bis(indolyl)methanes (BIMs) using Zeolite A as the catalyst

To synthesize BIMs, indole (0.942 mmol) and aldehyde (0.471 mmol) were dissolved in ethanol (6 mL) in a 25 mL round-bottom flask. To initiate the reaction, acid-treated zeolite (ZA2/30, 4 mol%) was added, and the mixture was stirred at 60 °C for 24 h. The progress of the reaction was monitored periodically using TLC. Once the reaction was complete, the mixture was centrifuged and washed with ethanol (2 × 5 mL), and the collected supernatant was evaporated using a rotary evaporator. DCM (2 × 5 mL) was added to the residue, and the mixture was washed with water (2 × 5 mL). Evaporation of the DCM gave a crude product that was purified using column chromatography (hexane and ethyl acetate polarity gradient) as the mobile phase. The purified product was characterized using ^{1}H, ^{13}C NMR and HRMS techniques.

3. Results and discussion

3.1 Coal fly ash to ball-milled fly ash: characterization

Native fly ash (CFA) from the thermal power plant was characterized using XRD, FTIR, FE-SEM, and EDS. The results displayed compliance with our previous study, as reported by Mahajan *et al.*[34] The native CFA sample was acid-treated and calcinated to remove organic and inorganic impurities. This pretreated fly ash sample (P-FA) was ball-milled to obtain homogenously reduced particles (B-FA) for efficient fusion in subsequent steps and to enhance the surface area of the final product. A comparison of the XRD pattern (Fig. 3a) for the native CFA with a ball-milled sample (B-FA) showed the broadening of peaks in the latter case due to reduced crystallite size. The new peak at 48.5 2θ in the B-FA sample was due to Al_2O_3 (ICDD card no. 01-073-1199), as ball milling caused the breakage of particles and oxidation of surface aluminium.
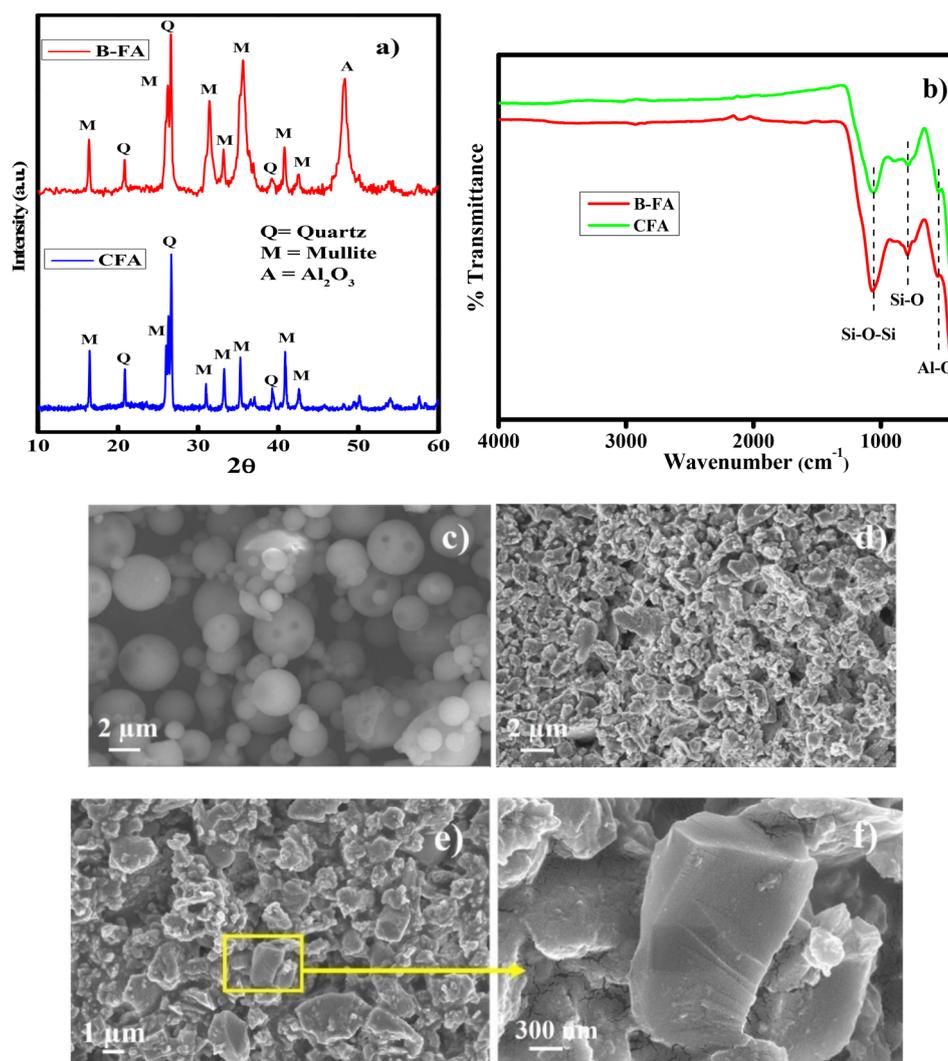

Fig. 3 (a) XRD patterns of coal fly ash (CFA) and ball–milled fly ash (B–FA), where the peak broadening in B–FA indicates a reduction in crystallite size. (b) FTIR spectra for CFA and B–FA indicate that native bonds remain intact after ball milling. (c) FE-SEM image of native CFA and (d) B–FA shows a transition from spherical to an irregular shape after the ball-milling process. (e) At 1 μm resolution and at (f) 300 nm resolution, the transformation into shattered, irregularly shaped particles is clear.

FTIR spectra (Fig. 3b) displayed no change or shift in the peaks from CFA to B-FA, indicating that native bonds remained intact after pretreatment and ball milling. The FE-SEM images of CFA (Fig. 3c) and B-FA (Fig. 3d–f) displayed a transition from spherical to irregularly shaped particles after the ball-milling process. At 1 μm (Fig. 3e) and 300 nm (Fig. 3f) resolutions, native spherical particles (CFA) were transformed into shattered, irregularly shaped particles.

3.2 Characterization of the synthesized Zeolite A (ZA)

The ball-milled fly ash (B-FA) was processed to synthesize Zeolite A using an ultrasonication-assisted hydrothermal method. The hydrothermal process was carried out at 90 °C for 6, 8, 10, and 12 h to optimize the crystallization conditions. The XRD spectra (Fig. S1) show that as the time increased from 6 to 10 h, the amorphous phase gradually transformed into pure-phase ZA. This was evident from the complete disappearance of the characteristic amorphous hump after 10 h. Increasing the reaction time to 12 h led to the appearance of an additional crystalline phase, identified as Faujasite-Na (ICDD card no. 00-012-0246), which coexisted with zeolite A. Crystallinity analysis also confirmed that ZA-10H exhibits the highest crystallinity (Section S1). Thus, the hydrothermal treatment of 10 h was determined to be optimal for obtaining pure-phase zeolite A (Fig. 4a), which was designated as ZA and used for further characterization and catalytic studies.

The XRD pattern of the synthesized material (ICDD card number 01-089-3859) and the absence of quartz and mullite peaks in the fly ash confirmed the formation of ZA.[37] A significant shift of the T–O–T bond (where T = Si or Al), in the FTIR spectra (Fig. 4b) from 1062 cm^{-1} to 966 cm^{-1}, confirmed a structural change resulting from the rearrangement of Si and Al bonds.[6] The FE-SEM images of the synthesized material (Fig. 4c and d) compared with B-FA (Fig. 3d) show an evident change from a rough, irregular to a smooth cubic morphology, confirming the synthesis of ZA with an average size of 1.7 μm.[35] EDS data (Table 1) of the synthesized material displayed Si and Al present in equal amounts, further confirming pure phase ZA. These results also show that Na is present as a counterion in the zeolite framework.

As discussed above, the use of ZA was explored for the synthesis of medicinally important BIMs. The initial results in the presence of ZA using indole and benzaldehyde in ethanol at 60 °C for 24 h gave 28% yield for compound **3a**, where R = C$_6$H$_5$ (Fig. 1). Although the yield was relatively low, the positive reports in the literature on acid-treated zeolites with enhanced surface area and organic reaction yields were the driving force to take up the acid modification of ZA.[29,38,39]

3.3 Modification of ZA

Scheme 1(a) shows the modification of ZA with different concentrations of HCl to obtain three samples: ZA1, ZA2, and ZA3.
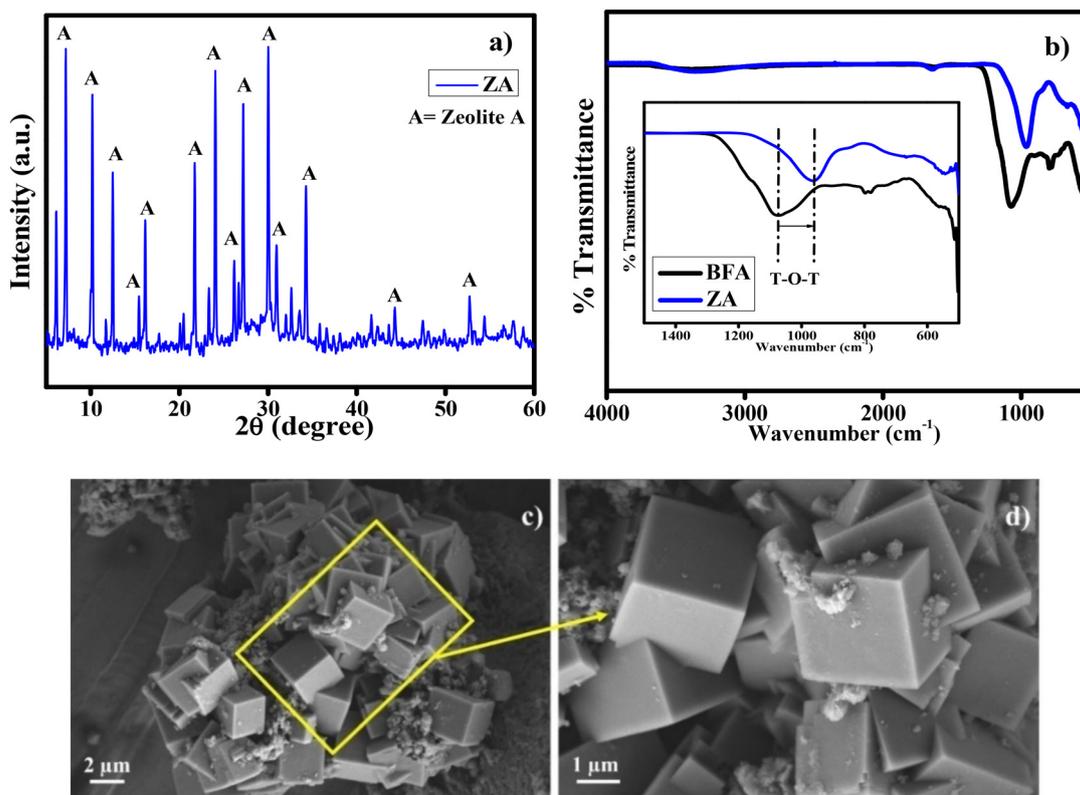

Fig. 4 (a) The absence of quartz and mullite peaks in the XRD pattern confirms the formation of Zeolite A (ZA). (b) FTIR analysis of ZA compared to B-FA shows a shift in the peak from 1062 cm^{-1} to 966 cm^{-1} attributed to the rearrangement of Si and Al bonds. (c) FE-SEM images of ZA reveal a smooth cubic morphology, confirming ZA formation at 2 μm and (d) 1 μm resolution.

Table 1   EDS analysis showing the atomic percentages of constituent elements in FA, B-FA, ZA, ZA2/30, and ZA2/90

		Elements (atomic percentage)											
	Samples	Ti	Al	Si	C	O	K	Ca	Mg	Fe	Na	W	Si/Al
Raw fly ash	FA	0.31	13.91	14.99	8.12	58.99	1.16	0.36	0.63	1.39	—	—	1.07
	B-FA	0.42	9.14	11.65	27.87	49.14	0.48	—	—	0.75	—	0.56	1.2
Synthesized Zeolite	ZA	0.26	9.68	9.46	16.40	53.00	—	—	—	0.56	10.63	—	0.97
	ZA2/30	0.29	11.21	10.51	14.17	57.15	—	—	—	0.57	6.47	—	0.93
	ZA2/90	0.30	10.56	9.58	16.58	59.16	—	—	—	0.56	3.26	—	0.90
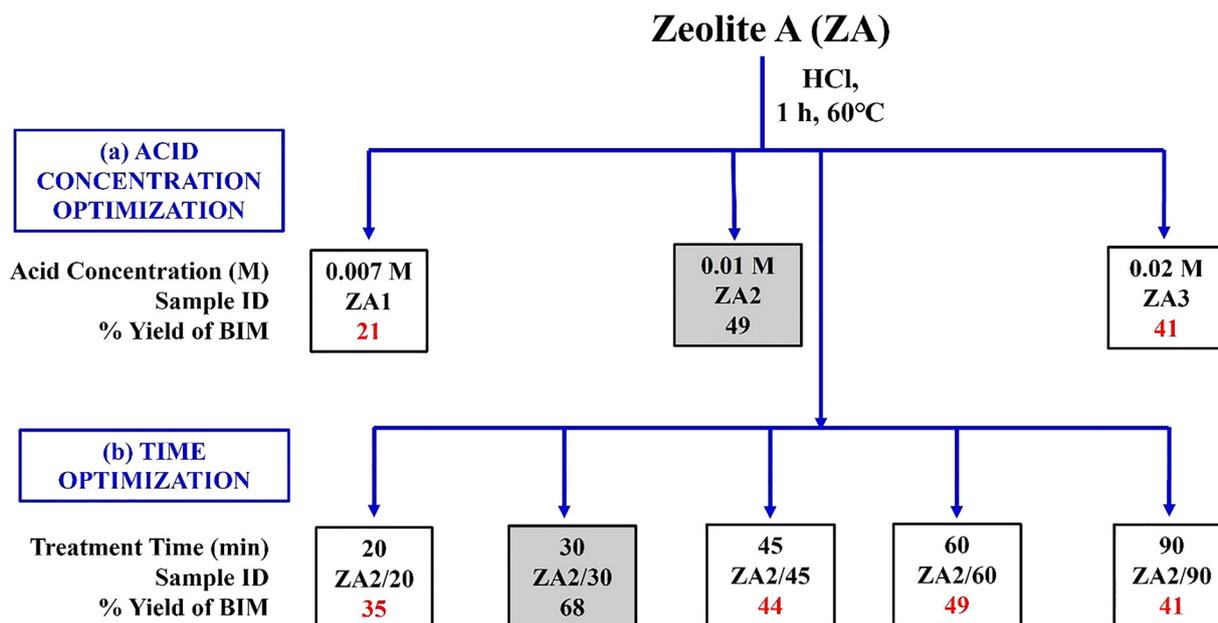
Scheme 1   (a) Post-synthetic modification of ZA with HCl at different concentrations under constant time and temperature gave the most efficient catalyst (ZA2), affording 49% yield of BIMs. (b) Treatment of ZA with 0.01 M HCl for different durations gave an optimum reaction time of 30 min, providing the maximum yield of BIMs (68%) with ZA2/30.

A maximum yield (49%) of the compound **3a**, a BIM, was obtained in the case of ZA2, which was achieved by treating ZA with 0.01 M HCl for 1 h. The other two samples, ZA1 and ZA3, treated with 0.007 M and 0.02 M HCl, yielded 21% and 41%, respectively. Furthermore, to optimize the time interval for the HCl treatment, ZA was treated with 0.01 M HCl at 20, 30, 45, and 90 minutes before being used for the synthesis of compound **3a**. Scheme 1(b) further shows that ZA was treated with 0.01M HCl for 30 min, named ZA2/30, which gave the maximum yield (68%) as compared to others treated for 20 (ZA2/20), 45 (ZA2/45), 60 (ZA2/60), and 90 (ZA2/90) minutes. After optimization, ZA2/30 was the final material that was used to explore the synthesis of other BIMs. Therefore, the characterization of the ZA2/30 was carried out. To understand the reaction mechanism, characterization studies of ZA2/30 were compared with those of ZA2/90.

3.4   Characterization of acid-treated zeolites

The XRD of native ZA, ZA2/30, and ZA2/90 (Fig. 5a) was analyzed to evaluate structural changes due to acid treatment. With increased treatment time, the material lost crystallinity as evidenced by a reduction in peak intensity. For ZA2/90, the graph shows a broad hump, suggesting an increase in the amorphous phase with prolonged acid treatment. These results suggested that a 30 min treatment with acid was optimal for preserving the framework of the zeolite.

Fig. 5b compares the FTIR spectra of ZA with acid-treated samples (ZA2/30 and ZA2/90) to check structural stability and surface modifications. The band at 3339 cm^{-1}, corresponding to surface −OH groups, increased after 30 min of treatment but decreased after 90 min compared to native ZA. This indicated that ZA2/30 has maximum Brønsted acid sites compared to ZA and ZA2/90. A comparison with the XRD results indicated that the intensity of the OH peak decreased due to structural deformation in the case of ZA2/90. A similar trend corresponding to H−O−H bending vibrations was observed at 1639 cm^{-1} due to surface-adsorbed water molecules.[40] The bands at 959 and 854 cm^{-1}, corresponding to T−O−T vibrations and Si−O−Al linkages from the crystalline mullite phase, shifted to 974 and 869 cm^{-1}, respectively, upon acid treatment. The bands at 647 cm^{-1} (Si−O−Si) and 860 cm^{-1} (Al−O−Si) remained intact, confirming that the framework was not deformed.
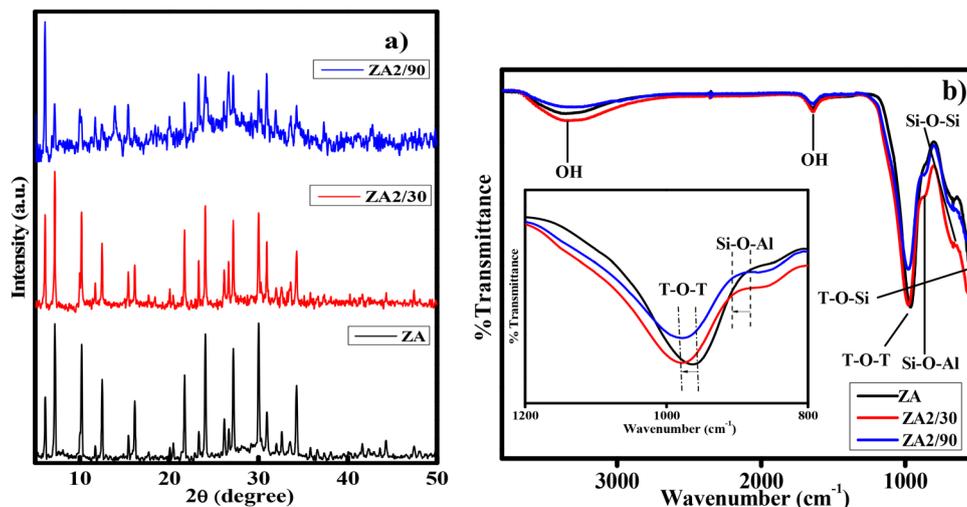
Fig. 5 (a) XRD of ZA, ZA2/30, and ZA2/90 showing loss of crystallinity with increasing acid treatment. ZA2/30 retains the framework, while ZA2/90 shows an increase in the amorphous nature. (b) Comparative FTIR spectra of the three samples reveal that while the T−O−T (T = Si, Al) bonds remained intact, the decreased intensity of the OH peak in the case of ZA2/90 indicates structural deformation.

Hence, the FTIR analysis of the materials confirmed that mild treatment (30 min) helped enhance surface hydroxy groups without any damage to the framework.

Fig. 6 demonstrates the FE-SEM images of acid-treated samples, ZA2/30 and ZA2/90. A 30 min acid treatment eroded the fine edges of original cubic crystals of ZA (Fig. 4c and d) into rougher ones (ZA2/30, Fig. 6a and b). Furthermore, a prolonged 90 min acid treatment severely degraded and deformed the crystals (ZA2/90, Fig. 6c and d), indicating deterioration of the framework.

The point of zero charge (PZC) of native ZA and acid-treated samples (ZA2/30, ZA2/90) was determined by the salt addition method. As shown in Fig. 7a, increasing acid treatment shifted the PZC from pH 7.6 (ZA) to 7.2 (ZA2/30) and further to 6.9 (ZA2/90). This indicates that prolonged acid treatment enhances the surface acidity of the zeolite.

The TGA data (Fig. 7b) show that the highest mass loss was for ZA2/30 (19%), followed by ZA2/90 (17.4%) and ZA (16.1%). The major weight loss was observed below 200 °C, beginning at ∼100 °C, for all samples, indicating that materials were
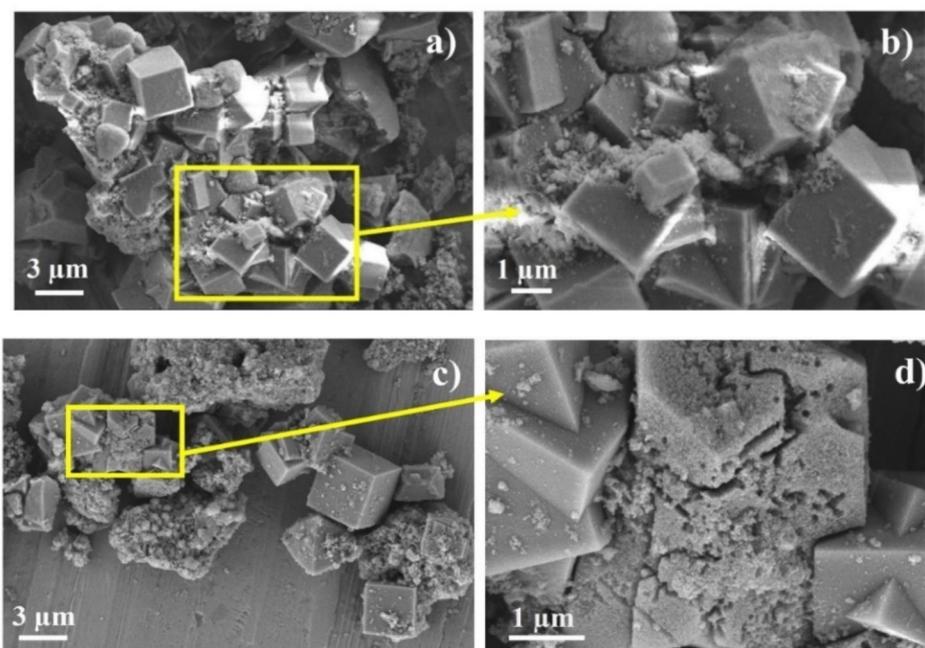

Fig. 6 FE-SEM images of (a) and (b) ZA2/30 (30 min acid treatment) and (c) and (d) ZA2/90 (90 min acid treatment) reveal surface roughening and framework deterioration with increasing treatment time.
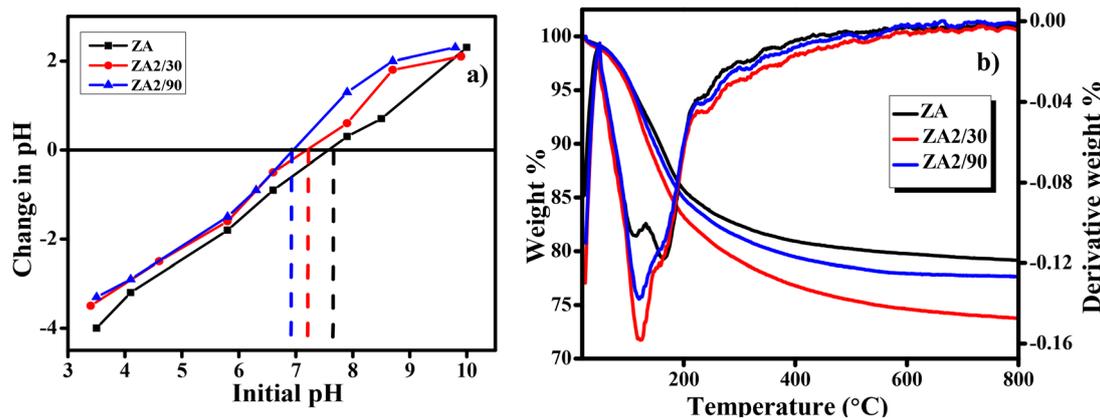
Fig. 7 (a) Comparison of ZA and acid-treated samples (ZA2/30 and ZA2/90) reveals that the point of zero charge (PZC) shifts from pH 7.6 to 6.9, suggesting that prolonged acid treatment enhances the surface acidic characteristic of the zeolite. (b) Comparative TGA analysis of three samples shows the highest mass loss for ZA2/30, indicating its higher surface area and improved pore accessibility.

thermally stable at higher temperatures. DTG profiles also displayed two peaks for ZA at 115 °C and 167 °C, corresponding to surface-adsorbed and pore-confined water molecules.[41,42] For ZA2/30, DTG indicated that the sample exhibited a higher surface area, as reflected by the sharp DTG peak at 120 °C. The transition from the second peak to the shoulder for ZA2/30 indicated that larger pores facilitated the easier release of pore water at lower temperatures (162 °C) compared to ZA (167 °C). In contrast, prolonged acid treatment for 90 min, (ZA2/90) displayed diminished DTG peaks and reduced porosity, consistent with XRD and SEM evidence of framework degradation.

BET analysis further corroborated these results. Both samples ZA and ZA2/30 exhibited type II isotherms with H3 hysteresis loops, characteristic of slit-shaped mesopore particles[35] (Fig. 8). Acid treatment for 30 min increased the surface area (Fig. 8a) from 56.1 to 66.2 $m^2 g^{-1}$ and the average pore size (Fig. 8b) from 5.4 to 6.3 nm (ZA to ZA2/30), confirming the enhancement of porosity upon acid treatment. These results were further validated by EDS and XPS analyses.

To ensure the safety of the material for any further application, EDX analysis was performed at all stages of the zeolite

optimization. The data in Table 1 show the progression of material transformation from raw fly ash (FA) to acid-treated zeolite (ZA2/90). It was observed that K, Ca and Mg were eliminated following ball milling and washing. Fe, on the other hand, decreased during the ball milling and remained constant after ZA formation. In the case of B-FA, W was introduced from the ball mill but was subsequently removed during further treatments. The analysis of ZA shows a Si : Al ratio of 0.97, which decreases to 0.93 and 0.90 after 30 and 90 minutes of acid treatment, respectively, indicating an increase in the Al percentage. Additionally, Na ions, which were introduced during the conversion of ball-milled fly ash to ZA, were effectively removed upon acid treatment, as their atomic percentage decreased from 10.63 to 3.26, while the percentage of O increased. These changes collectively indicate significant structural modifications in the zeolite framework induced by acid treatment.

High-resolution XPS studies were carried out to investigate the surface chemical states and elemental composition of the synthesized zeolites. The deconvoluted spectra (Fig. S2) and the corresponding quantitative results are summarized in Table 2.
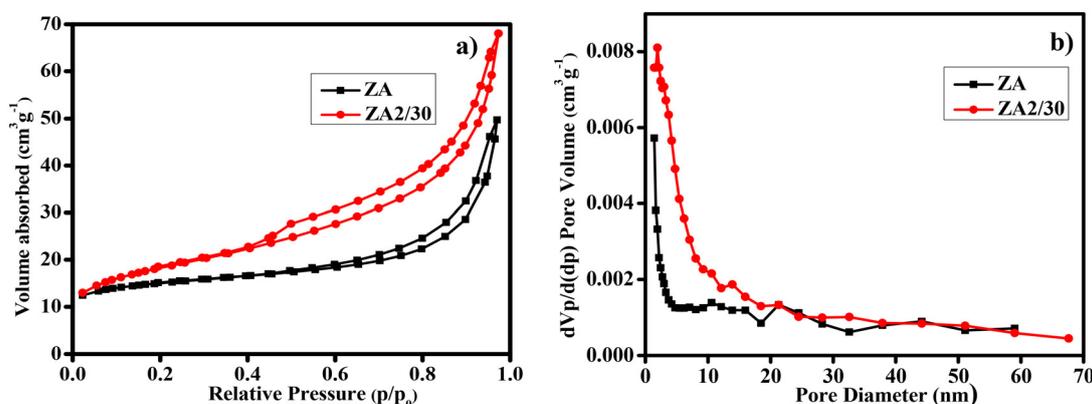

Fig. 8 (a) N₂ absorption and desorption isotherm and (b) pore size distribution reflecting enhanced surface area and pore size for ZA2/30 compared to ZA.

For O 1s, the zeolites displayed multiple peaks corresponding to different oxygen environments (O^{2-}, Al_2O_3/C=O, Si–O–Si/Al–OH, C–OH, Si–OH, and H_2O/O_2).[43] The total atomic percentage after 30 min of acid treatment (ZA2/30) showed an increase in O^{2-} and C–OH contents while reducing Si–O–Si/Al–OH, Si–OH, and H_2O/O_2. For C 1s, a decrease in C–Si and an increase in C=C bonds were observed after acid treatment.[44,45] Si 2p spectra showed peaks for Si–C, Si–O, and SiO_2.[46] Upon acid treatment, the atomic percentage for the Si–O bond decreased from 44.0 to 39.4%, attributed to the breaking of Si–O–Al bonds, while SiO_2 increased from 23.3 to 29.2%. Similarly, the Al 2p spectra revealed the Al–O (84.1%) framework and Al–OH (15.8%) extra-framework, which, after 30 min acid treatment, shifted to 95.1% Al–O and 4.8% Al–OH, confirming the formation of new Al–O bonds and loss of Al–OH.[47] Na atomic percentage decreased from 4.44 to 1.38 (Table 2), reflecting sodium leaching and contributing to increased surface acidity.[48] Thus, the high-resolution XPS analysis confirms that ZA, after 30 minutes of acid treatment, induces significant bond reorganization, leading to a rearrangement of the zeolite framework.

Previous studies have demonstrated that Al removal and subsequent reinsertion occur during the acid treatment of zeolites, thereby inducing structural changes on their surfaces.[49–51] These findings support the structural changes in the framework of ZA upon acid treatment to obtain ZA2/30, justifying the decrease in the Si:Al atomic ratio from 1.5 (ZA; Si: 16.70%, Al: 10.93%) to 1.08 (ZA2/30; Si: 15.63%, Al: 14.45%), which also corroborates the EDS results.

To evaluate the strength and distribution of acid sites in zeolites, NH_3-TPD analysis was performed. Fig. 9 presents the NH_3-TPD profiles of the parent zeolite (ZA) and the acid-treated samples (ZA2/30 and ZA2/90). The desorption curves were deconvoluted using the Pearson VII function to determine the distribution of weak, moderate, and strong acid sites, as shown
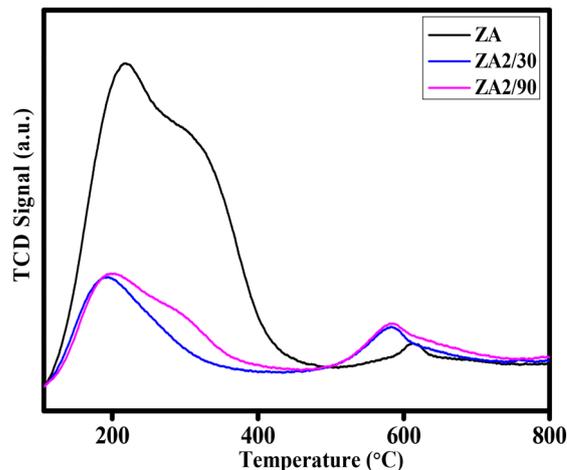

Fig. 9 NH_3-TPD data showing comparison of ZA with acid-treated samples.

in Fig. S3. The deconvoluted peak data (Table 3 and Fig. S3) revealed that acid treatment significantly modified both the number and strength distribution of the surface acid sites. The total acid sites and acidity were determined using the formula described in Section S4.1.

The parent ZA exhibited desorption primarily in the 100–250 °C range, corresponding to weak acid sites (39.04%), while moderate acid sites (50.06%) dominated in the 250–400 °C region. Only a small fraction (10.88%) of the strong acid sites desorbed above 450 °C.[52] After 30 min of acid treatment (ZA2/30), the proportion of strong acid sites increased markedly to 26.80%, accompanied by a rise in weak acid sites (44.36%) and a decrease in moderate sites (28.83%). However, prolonged treatment for 90 min (ZA2/90) was less favorable, as weak sites increased to 60.03%, while moderate and strong sites decreased to 19.86% and 20.10%, respectively, indicating progressive framework degradation. Overall, 30 min acid treatment (ZA2/30) yields an optimal balance of acid sites, enhancing its suitability for catalytic applications that require strong acidity.

Fig. 10 schematically illustrates the chemical transformations that occurred during acid treatment. The surface of the parent zeolite contained extra-framework Al–OH groups responsible for Lewis acidity and framework Si–O(H)–Al linkages that contributed to Brønsted acidity.[53] Upon acid exposure, both silicon and aluminum atoms were partially leached from the surface and bulk of the framework. However, XPS analysis revealed that only aluminum was reinserted into the framework, while the leached Si does not reincorporate, as evidenced by the overall decrease in the Si atomic percentage in Table 2. During the early stages of acid treatment, the loosely bound surface Al–OH species were preferentially removed compared to the Al atoms bonded within the bulk of the zeolite framework. This was supported by XPS data, which showed a decrease in the Al–OH component from 15% in ZA to 4.8% in ZA2/30 (Table 2).

Once aluminum was extracted from the zeolite, it formed $Al(OH)_2$ species, which were protonated in the acidic medium

Table 2 XPS parameters for the ZA and ZA2/30 samples obtained from the deconvoluted high-resolution spectra of C 1s, O 1s, Na 1s, Al 2p, and Si 2p after spectral fitting

Individual sample component	Group	ZA Total atomic %	ZA Atomic %	ZA2/30 Total atomic %	ZA2/30 Atomic %
C 1s	C–Si	22.76	18.1	20.34	11.3
	C=C		44.7		49.4
	C–O		11.3		12.1
	C=O		15.1		15.8
	O=C–O		10.5		11.2
O 1s	O2–	45.18	12.2	48.20	16.2
	C=O/Al_2O_3		17.0		17.4
	Si–O–Si/Al–OH		40.5		36.0
	C–OH		10.6		23.3
	Si–OH		15		5.6
	H_2O/O_2		4.4		1.09
Si 2p	Si–C	16.70	32.5	15.63	31.3
	Si–O		44		39.4
	SiO_2		23.3		29.2
Al 2p	Al–O	10.93	84.1	14.45	95.1
	Al–OH		15.8		4.8
Na 1s	Na	4.44	100	1.38	100

Table 3 Comparison of the total acid sites for ZA and modified zeolites (ZA2/30 and ZA2/90), along with the turnover number (TON) and turnover frequency (TOF), as determined from NH_3-TPD analysis

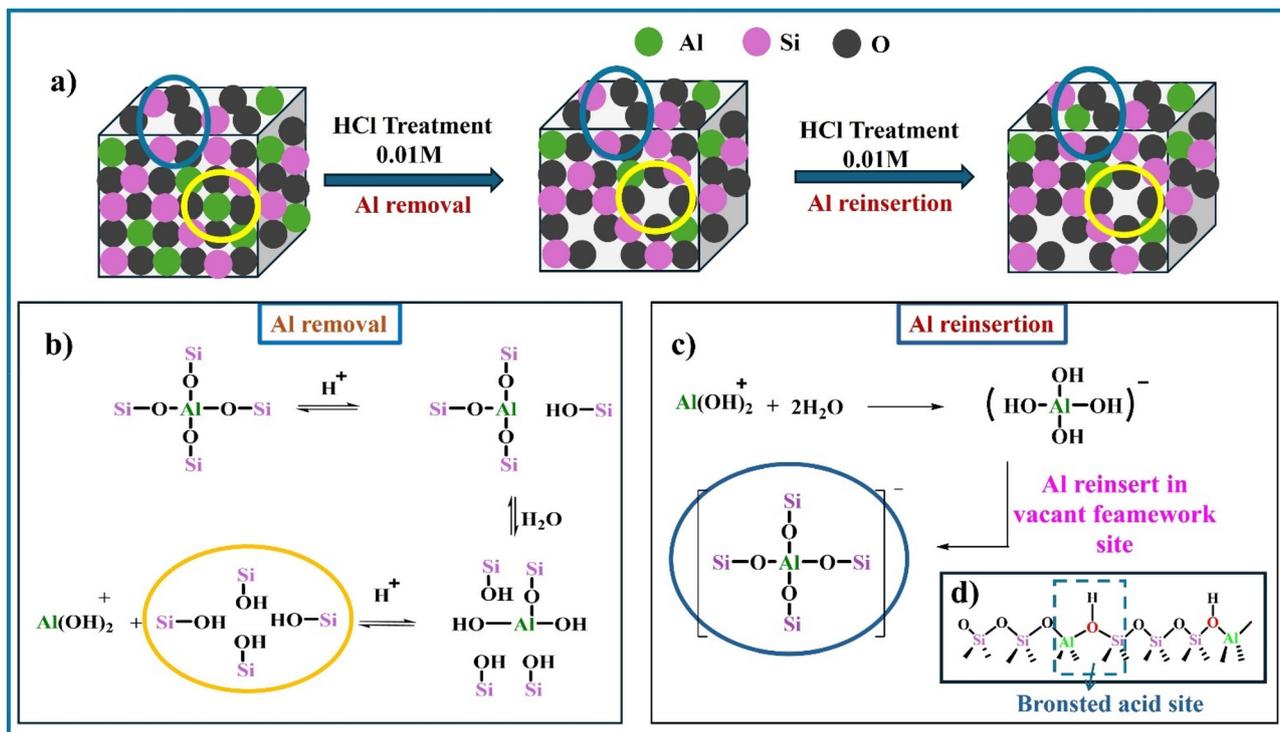| Sample ID	Weak acid site (%)	Moderate acid site (%)	Strong acid site (%)	Total acid site (mmol)	Acidity (μmol g^{-1})	TON	TOF (h^{-1})
ZA	39.04	50.06	10.88	0.0130	222.8	9.8	0.40
ZA2/30	44.36	28.83	26.80	0.0033	62.1	95.5	3.9
ZA2/90	60.03	19.86	20.10	0.0046	82.1	41.7	1.7

Fig. 10 (a) General scheme for aluminum removal and reinsertion. (b) Schematic equation showing removal of surface Al–OH groups with acid treatment, generating Al(OH)$_2^+$ species. (c) Al (OH)$_2^+$ species reinserts to occupy framework vacant surface sites to form [Si–O–Al]$^-$ species generating a (d) Brønsted site as shown in box Si–O(**H**)–Al.

to generate Al(OH)$_2^+$ ions. These ions migrated back and occupied the vacant framework sites, leading to the formation of new bridging Si–O(H)–Al linkages.[38,50] This conjecture is supported by XPS data, which show an increase in bonded Al–O from 84% in ZA to 95% in the case of ZA2/30. This reinsertion process enhanced the Brønsted acidity, as evidenced by the increased number of strong acid sites in the ZA2/30 sample (Table 3). Simultaneously, the loss of surface Al–OH groups accounted for the reduction in moderate and weak acid sites in ZA2/30 relative to the parent ZA.

Prolonged acid treatment (90 min) caused further dealumination and partial breakdown of the zeolite framework. This was confirmed by the characterization of the ZA2/90 sample, which, in comparison with ZA, showed degraded and deformed cubic morphology (Fig. 6), reduced –OH band intensity in the FTIR spectra, and lower peak intensities in the XRD patterns (Fig. 5). This structural degradation reduced the Si–O–Al connectivity and generated additional silanol (Si–OH) groups, consistent with the predominance of weak acid sites and the loss of strong Brønsted sites observed in the NH$_3$-TPD results (Table 3).

3.5 Catalyst application in organic synthesis

Many organic transformations typically require stoichiometric amounts of mineral or organic acids. Motivated by this, we envisioned utilizing the intrinsic acidity of ZA2/30 as a solid catalyst. The synthesis of BIMs was selected as a model reaction to evaluate the catalytic efficiency of the acid sites in the fly ash–derived zeolite.

BIMs were synthesized by reacting indole (2 equivalents) with benzaldehyde (1 equivalent) in the presence of ZA2/30. A control experiment, conducted without the use of a catalyst, showed no product formation, confirming the essential catalytic role of ZA2/30. The reaction was further optimized by varying catalyst loading, solvents, time, and temperature. Among the tested solvents (Table 4), ethanol proved to be the most effective, while dichloromethane, propanol, toluene, THF, and DMSO showed no product formation. Temperature studies revealed that the reaction proceeded only at 60 °C, with no conversion at room temperature. The reaction afforded yields of 20%, 40%, and 68% at 10, 16, and 24 h, respectively, confirming 24 h as the optimal reaction time for maximum

Table 4 Optimization of reaction conditions for the synthesis of BIM (**3a**) using 4 mol% of ZA2/30

Solvent	Yield[a] (%)	Dipole moment	Boiling point (°C)	LD50 (mL kg^{-1})
CH$_3$CH$_2$OH	68	1.68	78.3	22.6
CH$_3$OH	29	2.87	64.7	5.6
CH$_3$CH$_2$CH$_2$OH	NR	3.09	97.2	2.3
ACN	37	3.44	81.6	3.9
H$_2$O	17	1.87	100	>90
DCM	NR	1.60	39.7	1.6
DMSO	NR	4.10	189	17.9
Toluene	NR	0.31	110	6.4
THF	NR	1.75	66	3.6
H$_2$O : EtOH				
80 : 20	12	—	—	—
50 : 50	10	—	—	—

[a] Conditions: 60 °C, 24 hours; NR = no reaction.

yield. The reduced efficiency of ZA2/30 at 2 and 6 mol% (yielding only 20% and 40%, respectively) led to the identification of 4 mol% as the optimal loading to achieve maximum yield. Thus, the optimal conditions for BIM synthesis were found to be using ethanol at 60 °C for 24 h with 4 mol% of ZA2/30 to explore the substrate scope.

A diverse set of substituted aldehydes (Table 5), including electron-donating (methoxy, hydroxy), electron-withdrawing (nitro, cyano, and fluoro), and disubstituted groups, was selected to evaluate substrate scope and the influence of electronic and steric effects. As shown in Table 5, the yields of different BIMs varied from 44% to 94%, depending on the nature of the aldehyde substituents. Aldehydes containing electron-withdrawing groups gave enhanced yields as compared to electron-donating groups.

It is essential to note that ZA2/30 exhibits highly acidic sites, which strongly interact with the carbonyl carbon of aldehydes. When electron-withdrawing groups are attached, this interaction stabilizes the resulting carbocation (Fig. 11a), thereby enhancing the electrophilicity of the carbonyl centre.[54] As a result, aldehydes with electron-withdrawing substituents afforded higher yields than those with electron-donating groups (Fig. 11b), due to increased electrophilicity that facilitated attack by the C-3 position of the indole. Notably, aldehydes containing hydroxyl substituents yielded approximately 30% with inseparable side products under the applied conditions (not shown in Table 5), and the methoxy group gave only a 46% yield. Comparatively, cyano (**2d**) and nitro (**2e**, **2f**) groups gave enhanced yields of BIM **3d** (94%), **3e** (76%) and **3f** (80%). For the comparatively weak electron-withdrawing chloro group on aldehyde (**2c**), a moderate yield (63%) was observed, which increased to 72% when two chloro groups (**2h**) were present. Similarly, the presence of two electron-donating groups (methoxy and hydroxy) in the case of compound **2i** resulted in a lower yield (44%).
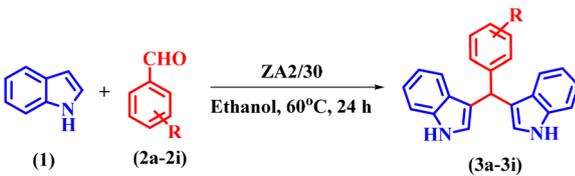
A comparison of the products from the monochlorinated aldehyde (**3c**) and the dichlorinated aldehyde (**3h**) reveals that substitution at the ortho and meta positions did not reduce the yield due to steric hindrance; however, a higher yield was obtained for **3h** instead (Table 5). This was attributable to the

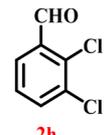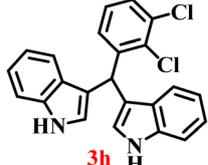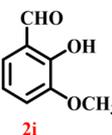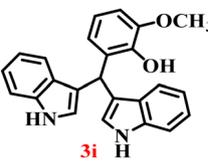**Table 5** Scheme for the synthesis of different BIMs with structures and yields using different aldehydes

R = Cl, OH, CN, NO$_2$, OCH$_3$, F, H

Entry	Aldehyde	Product	Yield (%)[a]
1.	2a	3a	68
2.	2b	3b	46
3.	2c	3c	63
4.	2d	3d	94
5.	2e	3e	76
6.	2f	3f	80
7.	2g	3g	90

Table 5 (continued)

R = Cl, OH, CN, NO$_2$, OCH$_3$, F, H

Entry	Aldehyde	Product	Yield (%)^a
8.	2h	3h	72
9.	2i	3i	44
10.	HCHO 2j	3j	68
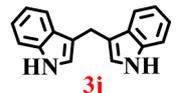
^{a} Isolated yield after purification.

Table 6 Synthesis of zeolite A from coal fly ash using different methods

Fusion	Aging	Hydrothermal conditions	Ref.
550 °C, 1 h	Stirring, 16 h	100 °C, 7 h	65
550 °C, 1 h	Incubated, 5 h	90 °C, 5 h.	66
750 °C, 2 h	Stirring, 12 h	75 °C, 18 h.	35
550 °C, 1 h	Incubator shaking, 16 h, 30 °C	100 °C, 1 h	67
750 °C, 2 h	3 h, RT, probe sonication	90 °C, 10 h.	This work

dominant electron-withdrawing effect of the two chloro groups. Similarly, the methoxy- (**3b**) and hydroxy, methoxy disubstituted (**3i**) aldehydes, bearing mono- and disubstituted electron-donating groups, afforded nearly identical yields (46% and 44%, respectively), further confirming that steric hindrance has little influence on the reaction outcome.

The synthesis of BIMs demonstrates a sustainable strategy for valorizing abundantly available coal fly ash through its zeolitization. The synthesized zeolite effectively promotes the formation of pharmaceutically important compounds **3b** and **3c** (Table 5), which have been reported to exhibit anticancer and antiparkinsonian activities, respectively.[55] The synthesis of

Arundine (**3j**), a natural bisindole alkaloid with potent anti-cancer properties, further underscores the pharmaceutical relevance of this approach.[56] It has been reported to inhibit the growth of colon (IC$_{50}$: 50–60 μM), prostate (IC$_{50}$: 20–40 μM), and breast (IC$_{50}$: 17–30 μM) cancer cells.[57–59] Interestingly, acetaldehyde and propionaldehyde produced negligible amounts of BIMs. This can be attributed to the fact that formaldehyde and benzaldehyde, owing to their higher polarity, interact more effectively with the zeolite surface, resulting in enhanced reactivity. The previous report also supports this trend, showing that zeolites catalyze reactions of aromatic aldehydes more efficiently than their aliphatic counterparts, thereby enabling selective reactivity.[60]

Thus, the dual outcome of waste valorization and its use in synthesizing bioactive molecules offers a greener alternative to conventional catalysts, which are often costly and non-renewable. Industrial-scale production of these important organic molecules would require further optimization of the synthesis conditions for ZA2/30 according to the production volume. This approach nonetheless indicates a shift towards reducing the environmental burden and promotes resource efficiency, directly supporting SDG 12 (responsible consumption and production).

3.6 Plausible mechanism of BIM synthesis using ZA2/30 as a catalyst

The higher density of strongly acidic sites, as indicated by NH$_3$-TPD analysis (Fig. 9 and Table 3), and the enhanced hydroxy peaks on ZA2/30 in FTIR (Fig. 5b), suggest the availability of
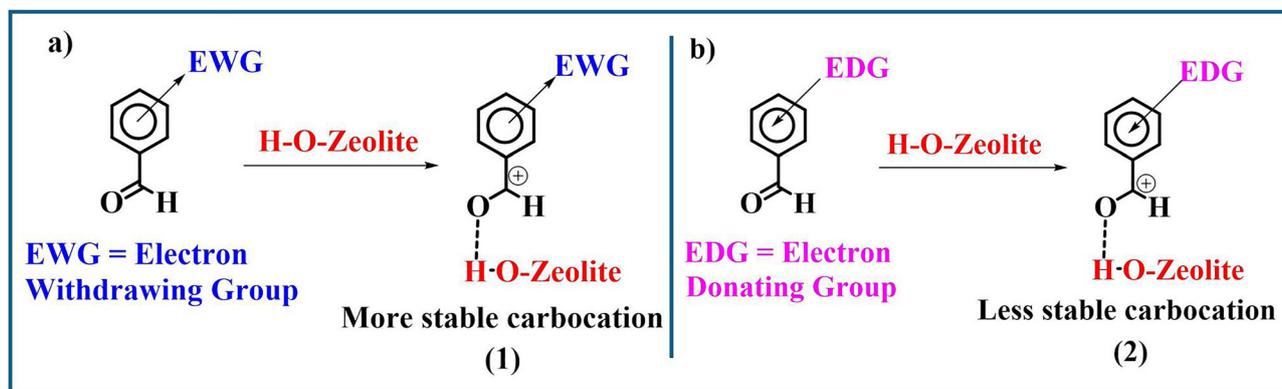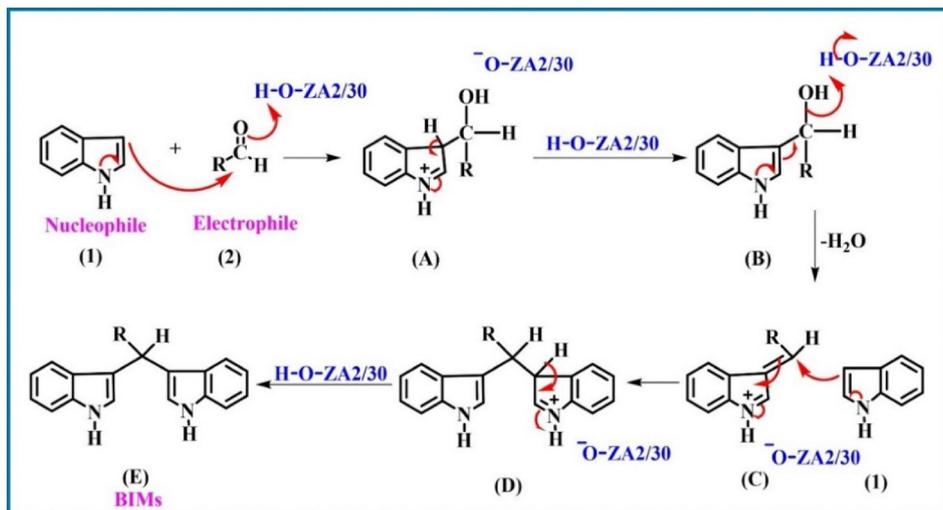

Fig. 11 (a) Electron-withdrawing substituents stabilize the carbocation, increasing carbonyl electrophilicity and resulting in higher BIM yields compared to (b) electron-donating groups.

Scheme 2 Mechanism of BIM formation: ZA2/30 activates benzaldehyde (2) for nucleophilic attack by indole (1) to form intermediate (B), which dehydrates to iminium ion (C) and reacts with a second indole to give the final product (E).

Brønsted acid sites that play a crucial role in the catalytic activity. The plausible reaction pathway is illustrated in Scheme 2. Initially, the acidic sites on ZA2/30 activate the carbonyl group of benzaldehyde (2), facilitating its nucleophilic attack by indole (1) to form intermediate (B). Subsequent dehydration of this intermediate produces the iminium ion (C), which then undergoes a second nucleophilic attack by another indole (1) molecule, resulting in the formation of the target BIM product (E). Notably, in the absence of ZA2/30, the starting materials remained unreacted, confirming the essential catalytic role of ZA2/30 in the transformation.

To further confirm that Brønsted acid sites were primarily responsible for the catalytic activity of the zeolite, ZA2/30 was treated with NH_4OH solution. After washing with water and drying at 80 °C, it was again employed for the synthesis of BIMs. The experiment did not give product formation, as confirmed by TLC (Fig. S6). This indicated the role of the Brønsted acid sites in BIM synthesis, which, after being poisoned by NH_3, did not give the desired product. Jacobs et al. have shown the role of ammonia in blocking the Brønsted acid sites of zeolites to form stable NH_4^+ species through proton transfer, thereby neutralizing these active sites.[61]

3.7 Recyclability and leaching studies of ZA2/30

The catalyst ZA2/30 demonstrated reusability in the synthesis of BIMs (compound **3a**), retaining stable catalytic activity for up to five consecutive cycles (Fig. 12). To confirm the activity of the catalyst after its use in organic reactions, a post-reaction evaluation was carried out using XRD and FE-SEM. The XRD pattern of the recycled ZA2/30 showed no noticeable shift or broadening of peaks (Fig. S7a) compared with the fresh ZA2/30 sample. Likewise, FE-SEM images of the fresh catalyst ZA2/30 (Fig. 6a and b) and the recycled ZA2/30 (Fig. S7b) revealed no significant morphological deterioration, confirming that ZA2/30 maintained its crystalline structure and characteristic cubic framework. To evaluate the heterogeneous nature of
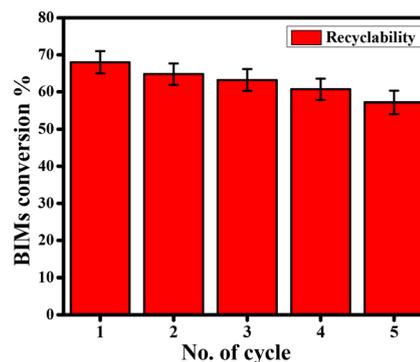

Fig. 12 Recyclability studies of zeolite (ZA2/30) for the synthesis of BIMs up to five cycles.

ZA2/30 as a catalyst, the reaction mixture was separated from the catalyst. After evaporation of the solvent, the sample was treated with HCl and diluted with water. MP-AES analysis revealed the presence of 0.047% Al and 0.05% Si, well below the permissible limit as reported in the literature.[62,63] These results clearly establish the robustness of ZA2/30 in terms of its structural integrity and catalytic efficiency for the organic transformations.

3.8 Turnover number (TON) and turnover frequency (TOF)

The catalytic performance of ZA2/30 was further evaluated in terms of TON and TOF (Table 3) using NH_3-TPD results as shown in Section S4.2. Acid treatment was found to significantly enhance the catalytic efficiency, with ZA2/30 exhibiting a TON (102.5) and TOF (4.27) that are nearly way higher than those of the parent ZA (11.21 and 0.46). ZA2/90, in contrast, displayed moderate activity (TON 44.9, TOF 1.8). In conclusion, ZA2/30 shows good catalytic activity and reusability, with structural and morphological stability maintained over repeated use and negligible metal leaching, confirming its robustness as a stable heterogeneous catalyst.

Table 7 BIM synthesis using commercially available zeolites compared to fly ash-derived zeolite A

Commercial Zeolite	Treatment	Solvent	BIMs yield (%)	Ref.
HY	—	CH_2Cl_2, RT	85	32
Hβ, HY, and H–ZSM-5	Zn^{2+} ion exchange	CH_2Cl_2, RT	85	33
HY, Hβ, and H–ZSM-5	—	CH_2Cl_2, RT	85	31
Hβ	Citric acid	Fixed bed reactor at 120 °C	90	30
Hβ and MCM-41	Lactic acid	CH_2Cl_2 at 30 °C	97	29
Coal fly ash-derived Zeolite A (non-commercial, lab synthesized)	Hydrochloric acid	Ethanol, 60 °C	94	This work

3.9 Literature comparison of Zeolite A synthesis from fly ash

This work presents a faster and more sustainable route for zeolite A synthesis from coal fly ash. Unlike earlier methods (Table 6), which require 5–16 h of aging, the present protocol achieves precursor activation in just 3 h with probe sonication and uses hydrothermal processing at moderate temperature. High-temperature fusion ensures complete conversion of fly ash, while sonication provides an energy-efficient alternative to prolonged incubation. By reducing time, energy, and reliance on commercial zeolites, this method ensures waste valorization and cost-efficient catalyst preparation, aligning primarily with SDG 12 (responsible consumption and production) and secondarily with SDG 7 (affordable and clean energy).

3.10 Comparing commercial and fly ash–derived Zeolite (ZA2/30) for BIM synthesis

BIM synthesis has been mostly reported using commercial zeolites (HY, Hβ, H-ZSM-5, Table 7) with dichloromethane ($LD_{50} \sim 1.6$ mL kg^{-1}), yielding up to 97% of the product. In this work, coal fly ash–derived zeolite A (ZA2/30) was used with a green and sustainable solvent, ethanol (LD50 ~ 22.5 mL kg^{-1})[64] to achieve yields comparable to those already reported (Table 7). The atom economy remained high at 94.3%, consistent with earlier reports using the same reactants for zeolite-based systems. The process mass index (PMI) and E-factor for our protocol were 30.9 and 29.9, respectively (Section S8), and are comparable to those of similar studies.[29,31–33] The larger PMI value reflects differences in mass efficiency; it does not diminish the broader advantages of our ethanol-based system in terms of lower toxicity, greater sustainability, and biodegradability. Overall, our approach combines waste valorization with the use of benign solvents to reduce environmental impact while maintaining catalytic efficiency, providing a more sustainable alternative to conventional methods.

4. Conclusion

The present study demonstrates the successful valorization of coal fly ash into Zeolite A, establishing an eco-friendly and sustainable application. Acid treatment enhanced the catalyst, with ZA2/30 exhibiting superior physicochemical properties and a well-defined crystalline framework characterized by an enhanced surface area, porosity, and acidity. These features enabled high catalytic activity, affording moderate to excellent yields of various BIM derivatives, including the synthesis of the bioactive natural product Arundine. The stable performance over five reuse cycles further confirmed the robustness of the catalyst. However, the scope of this catalytic system can be further expanded by exploring a wider range of nucleophiles and improving its applicability through reduced reaction times, which can be achieved by optimizing catalyst loading in combination with energy-efficient techniques such as microwave or ultrasound irradiation. Beyond these optimizations, the approach also holds promise for diverse catalytic reactions that can lead to valuable industrial compounds relevant to pharmaceutical and petrochemical sectors. Further studies may be required to evaluate the long-term stability of the zeolite under various storage conditions (pH, moisture, and other environmental factors). Additionally, any potential toxicity arising from residual fly ash–derived impurities, depending on their source, particularly in pharmaceutical applications, needs to be addressed. Overall, the work underscores the dual potential of fly ash-derived zeolites in environmental remediation and fine chemical synthesis, evidencing circular chemistry practices.

Author contributions

Aashima Mahajan: conducted experiments, collected and analyzed data, and prepared the original manuscript draft. Dr Loveleen K. Brar: supervised material synthesis and optimization, guided data interpretation, and contributed to manuscript editing. Dr Manmohan Chhibber: supervised organic reactions, supported characterization and data interpretation, and contributed to manuscript editing.

Conflicts of interest

There are no conflicts of interest to declare.

Abbreviation

CFA	Coal fly ash
P-FA	Pretreated fly ash
B-FA	Ball-milled fly ash
ZA	Zeolite A
ZA1	Zeolite A HCl treatment at 0.007 M, 1 h
ZA2	Zeolite A HCl treatment at 0.01 M, 1 h
ZA3	Zeolite A HCl treatment at 0.02 M, 1 h
ZA2/20	Zeolite A (0.01 M) HCl treated for 20 min
ZA2/30	Zeolite A (0.01 M) HCl treated for 30 min

ZA2/45	Zeolite A (0.01 M) HCl treated for 45 min
ZA2/60	Zeolite A (0.01 M) HCl treated for 60 min
ZA2/90	Zeolite A (0.01 M) HCl treated for 90 min
BIMs	Bis(indolyl)methane derivatives
TON	Turnover number
TOF	Turnover frequency
MP-AES	Microwave plasma–atomic emission spectroscopy

Data availability

The data supporting the findings of this study are available from the corresponding author upon request. All the data generated or analyzed during this study are included in this article and its supplementary information (SI). Supplementary information is available. See DOI: https://doi.org/10.1039/d5ma00772k.

Acknowledgements

References

1 J. D. Alonso, X. Gaviria, J. E. López and J. F. Saldarriaga, *Environ. Dev. Sustain.*, 2024, **26**, 31677–31701.

2 Y. Chen, Y. Fan, Y. Huang, X. Liao, W. Xu and T. Zhang, *Ecotoxicol. Environ. Saf.*, 2024, **269**, 1–16.

3 S. S. Alterary and N. H. Marei, *J. King Saud Univ., Sci.*, 2021, **33**, 101536.

4 M. Shen, X. Jiang, M. Zhang and M. Guo, *J. Sol-Gel Sci. Technol.*, 2020, **93**, 281–290.

5 K. M. Rambau, N. M. Musyoka, R. Panek, W. Franus, M. Wdowin and N. Manyala, *Mater. Today Commun.*, 2021, **27**, 102433.

6 B. Makgabutlane, L. N. Nthunya, E. N. Nxumalo, N. M. Musyoka and S. D. Mhlanga, *ACS Omega*, 2020, **5**, 25000–25008.

7 C. Rodwihok, M. Suwannakeaw and K. Charoensri, *Bioresour. Technol.*, 2021, **331**, 125060.

8 A. S. Yusuff, A. K. Bhonsle, J. Trivedi, D. P. Bangwal, L. P. Singh and N. Atray, *Renewable Energy*, 2021, **170**, 302–314.

9 A. Mekki, A. Benmaati, A. Mokhtar, M. Hachemaoui, F. Zaoui, H. Habib Zahmani, M. Sassi, S. Hacini and B. Boukoussa, *J. Inorg. Organomet. Polym. Mater.*, 2020, **30**, 2323–2334.

10 G. Amariei, L. Valenzuela, A. Iglesias-juez, R. Rosal and M. Visa, *J. Environ. Chem. Eng.*, 2022, **10**, 107603.

11 N. Wang, X. Sun, Q. Zhao and P. Wang, *Chem. Eng. J.*, 2021, **406**, 126734.

12 S. Boycheva, A. Szegedi, K. Lazar, C. Popov and M. Popova, *Catal. Today*, 2023, **418**, 114109.

13 L. P. Lingamdinne, R. Kulkarni, Y. Ryu, S. H. Kim, M. S. Yoon, S. J. Won and J. R. Koduru, *New J. Chem.*, 2025, 15457–15469.

14 P. L. Tran-nguyen, K. Ly, L. Huynh and V. Thanh, *J. Taiwan Inst. Chem. Eng.*, 2021, **123**, 1–8.

15 Y. Zhou, A. Galarneau, J. Rodriguez, M. Opanasenko and M. Shamzhy, *Mater. Adv.*, 2024, **5**, 3207–3219.

16 A. Khaleque, M. M. Alam, M. Hoque, S. Mondal, J. Bin Haider, B. Xu, M. A. H. Johir, A. K. Karmakar, J. L. Zhou, M. B. Ahmed and M. A. Moni, *Environ. Adv.*, 2020, **2**, 100019.

17 A. Martins, V. Neves, J. Moutinho, N. Nunes and A. P. Carvalho, *Microporous Mesoporous Mater.*, 2021, **323**, 111167.

18 P. Bai, P. Wu, W. Xing, D. Liu, L. Zhao, Y. Wang, B. Xu, Z. Yan and X. S. Zhao, *J. Mater. Chem. A*, 2015, **3**, 18586–18597.

19 Z. Wu, Z. He, Y. Xu, J. Wang, X. Lu, Q. Xia and D. Zhou, *J. Porous Mater.*, 2021, **28**, 1041–1048.

20 S. Imran, M. Taha and N. Ismail, *Curr. Med. Chem.*, 2015, **22**, 4412–4433.

21 K. A. Chavan, M. Shukla, A. N. S. Chauhan, S. Maji, G. Mali, S. Bhattacharyya and R. D. Erande, *ACS Omega*, 2022, **7**, 10438–10446.

22 H. T. D. Nguyen, T. T. Nguyen, P. T. K. Nguyen and P. H. Tran, *Arabian J. Chem.*, 2020, **13**, 1377–1385.

23 Y. Fu, Z. Lu, K. Fang, X. He, H. Xu and Y. Hu, *RSC Adv.*, 2020, **10**, 10848–10853.

24 K. Rathi, O. S. Tiwari, V. Rawat, J. L. Jat, D. K. Yadav and V. P. Verma, *Org. Biomol. Chem.*, 2024, **22**, 3287–3298.

25 M. Rani, D. Utreja, N. K. Dhillon and K. Kaur, *Russ. J. Org. Chem.*, 2022, **58**, 1527–1533.

26 B. Baghernejad, H. Naseri and O. Marvi, *Russ. J. Org. Chem.*, 2024, **60**, 147–151.

27 G. Kumar, A. Srivastava and V. P. Singh, *Dalton Trans.*, 2023, **52**, 3431–3437.

28 N. Azizi and M. Edrisi, *J. Mol. Liq.*, 2020, **300**, 112263.

29 G. Y. Bai, Z. Ma, L. Shi, T. Li, J. Han, G. Chen, N. Li and P. Liu, *Res. Chem. Intermed.*, 2012, **38**, 2501–2510.

30 G. Bai, Z. Ma, L. Shi, X. Lan, Y. Wang, J. Han, M. Qiu, H. Fu and P. Liu, *Appl. Catal., A*, 2012, **427–428**, 114–118.

31 M. Karthik, C. J. Magesh, P. T. Perumal, M. Palanichamy, B. Arabindoo and V. Murugesan, *Appl. Catal., A*, 2005, **286**, 137–141.

32 A. V. Reddy, K. Ravinder, V. L. N. Reddy, T. V. Goud, V. Ravikanth and Y. Venkateswarlu, *Synth. Commun.*, 2003, **33**, 3687–3694.

33 M. Karthik, A. K. Tripathi, N. M. Gupta, M. Palanichamy and V. Murugesan, *Catal. Commun.*, 2004, **5**, 371–375.

34 A. Mahajan, M. Chhibber and L. K. Brar, *New J. Chem.*, 2024, **48**, 13917–13926.

35 X. Ren, L. Xiao, R. Qu, S. Liu, D. Ye, H. Song, W. Wu, C. Zheng, X. Wu and X. Gao, *RSC Adv.*, 2018, **8**, 42200–42209.

36 M. Heryanto, B. Abdullah and D. Tahir, *J. Phys.: Conf. Ser.*, 2019, **1317**, 012052.

37 T. V. Ojumu, P. W. Du Plessis and L. F. Petrik, *Ultrason. Sonochem.*, 2016, **31**, 342–349.

38 X. Zaiku, C. Qingling, Z. Chengfang, B. Jiaqing and C. Yuhua, *J. Phys. Chem. B*, 2000, **104**, 2853–2859.

39 J. Li, H. Liu, T. An, Y. Yue and X. Bao, *RSC Adv.*, 2017, **7**, 33714–33725.

40 B. Fareed, F. Sher, S. Sehar, T. Rasheed, F. Zafar, M. Ameen and E. C. Lima, *Catal. Lett.*, 2022, **152**, 732–744.

41 J. Madhu, A. Santhanam, M. Natarajan and D. Velauthapillai, *RSC Adv.*, 2022, **12**, 23221–23239.

42 A. Jacas-Rodríguez, P. Rodríguez-Pascual, D. Franco-Manzano, L. Contreras, C. Polop and M. A. Rodriguez, *Sci. Eng. Compos. Mater.*, 2020, **27**, 236–244.

43 K. Szewczuk-karpisz and R. Panek, *J. Mol. Liq.*, 2022, **357**, 1–11.

44 K. Ajravat, S. Rajput and L. K. Brar, *Diamond Relat. Mater.*, 2022, **129**, 109373.

45 M. S. Chandrasekar and N. R. Srinivasan, *Ceram. Int.*, 2016, **42**, 8900–8908.

46 A. Kaur, P. Chahal and T. Hogan, *IEEE Electron Device Lett.*, 2016, **37**, 142–145.

47 J. R. C. Sousa, J. A. Torres, A. S. Giroto, A. V. P. S. Oliveira, P. H. M. Silva, F. L. Santos, G. D. Iga, C. Ribeiro and E. Nogueira, *J. Environ. Chem. Eng.*, 2023, **11**, 1–10.

48 W. Rongchapo, C. Keawkumay, N. Osakoo, K. Deekamwong, N. Chanlek, S. Prayoonpokarach and J. Wittayakun, *Adsorpt. Sci. Technol.*, 2018, **36**, 684–693.

49 T. Sano, Y. Uno, Z. B. Wang, C. H. Ahn and K. Soga, *Microporous Mesoporous Mater.*, 1999, **31**, 89–95.

50 K. Chen, J. Zhao, A. Li, G. Li, Q. Zhang and T. Xia, *Microporous Mesoporous Mater.*, 2022, **338**, 1–26.

51 R. L. Jinghong Ma, Yuhong Kang, Ning Ma, Wenming Hao and Yan Wang, *Mater. Sci. Polym.*, 2013, **31**, 19–24.

52 M. T. Jayakumari and C. K. Krishnan, *RSC Adv.*, 2024, **14**, 21453–21463.

53 S. R. Batool, V. L. Sushkevich and J. A. van Bokhoven, *J. Catal.*, 2022, **408**, 24–35.

54 R. Contreras and J. Andre, *Tetrahedron*, 2005, **61**, 417–422.

55 P. Saini, P. Kumari, S. Hazra and A. J. Elias, *Chem. – Asian J.*, 2019, **14**, 4154–4159.

56 B. U. Khuzhaev, S. F. Aripova and R. S. Shakirov, *Chem. Nat. Compd.*, 1994, **30**, 296–300.

57 A. Lerner, T. Napso, N. Azzam and F. Fares, *BioMed Res. Int.*, 2012, **2012**, 256178.

58 P. Emami and M. Ueno, *PLoS One*, 2021, **16**, 1–20.

59 X. Ge, S. Yannai, G. Rennert, N. Gruener and F. A. Fares, *Biochem. Biophys. Res. Commun.*, 1996, **228**, 153–158.

60 M. V. Joshi and C. S. Narasimhan, *J. Catal.*, 1991, **128**, 63–68.

61 R. A. van, S. W. P. J. H. Jacobs, J. W. de Haan and L. J. M. van de Veri, *J. Phys. Chem.*, 1993, **97**, 10394–10402.

62 S. Reports, Scientific Reports Article in Press Copper immobilized MIL-125-NH 2 as an efficient nanocatalyst for click reaction and synthesis of benzo [b] pyrans IN, 2025.

63 H. Gruber-woelfler, P. F. Radaschitz, P. W. Feenstra, W. Haas and J. G. Khinast, *J. Catal.*, 2012, **286**, 30–40.

64 E. T. Kimura, D. M. Ebert and P. W. Dodge, *Toxicol. Appl. Pharmacol.*, 1971, **704**, 699–704.

65 J. D. C. Izidoro, D. A. Fungaro, J. E. Abbott and S. Wang, *Fuel*, 2013, **103**, 827–834.

66 J. Park, K. Ahn, W. Lee and C. Lee, *Mol. Cryst. Liq. Cryst.*, 2019, **687**, 89–96.

67 J. Cheng and C. Gao, *Mater. Sci. Eng.*, 2019, **543**, 1–8.